Available online at www.sciencedirect.com

SciVerse ScienceDirect

Ceramics International 39 (2013) 8441–8451

CERAMICS INTERNATIONAL

www.elsevier.com/locate/ceramint

Synthesis and properties of V_2O_3–Fe_2O_3 magnetic ceramic nanostructures

Monica Sorescu[a,*], Tianhong Xu[a], Collin Wade[a], Johanna D. Burnett[b], Jennifer A. Aitken[b]

[a]Duquesne University, Department of Physics, 309 B Fisher Hall, Pittsburgh, PA 15282-0321, USA
[b]Duquesne University, Department of Chemistry and Biochemistry, Mellon Hall, Pittsburgh, PA 15282-1503, USA

Received 6 March 2013; received in revised form 5 April 2013; accepted 8 April 2013
Available online 16 April 2013

Abstract

$xV_2O_3 \cdot (1-x)Fe_2O_3$ ($x=0.1$, 0.3, 0.5, and 0.7) solid solutions were successfully synthesized by mechanochemical activation of V_2O_3 and α-Fe_2O_3 mixtures. The study aims at exploring the formation of solid solutions at the nanoscale, which is of crucial importance for catalysis and sensing applications. X-ray powder diffraction (XRD), Mössbauer spectroscopy, scanning electron microscopy (SEM), simultaneous differential scanning calorimetry and thermogravimetric analysis (DSC–TGA), and optical diffuse reflectance spectroscopy were combined for detailed studies of phase evolution of $xV_2O_3 \cdot (1-x)Fe_2O_3$ solid solution under the mechanochemical activation process. The Mössbauer studies indicated that the spectrum of the mechanochemically activated composites evolved from a sextet for hematite to sextets and a doublet upon duration of the milling process with vanadium oxide. Simultaneous DSC–TGA studies indicated that the thermal stability of V_2O_3-α-Fe_2O_3 composites varies with the ball-milling time due to the effect of V^{3+}–Fe^{3+} ion substitution and the continuous formation of a solid solution. SEM images of the formed solid solution confirmed the wide range distribution of particles sizes composed of nano-grains. Optical diffuse reflectance spectroscopy studies showed that the synthesized V_2O_3-α-Fe_2O_3 solid solution had semiconductor properties.

Keywords: A. Milling; B. Spectroscopy; C. Magnetic properties

1. Introduction

Hematite is one of the most used oxides, with various applications in scientific and industrial fields. It can be used as semiconductor compound [1], magnetic material [2], catalyst [3], and gas sensor [4].

The vanadium oxides form a fascinating class of materials that exhibit a large variety of structures with different physical and chemical properties. This diversity makes vanadium oxides technologically relevant and leads to various applications, such as light detectors, electrical and optical switching devices, as well as heterogeneous catalysis [5,6]. From fundamental research interest and wide application points of view, vanadium oxides possess various vanadium oxidation states ranging from +2 to +5 as well as different oxygen geometries in the crystalline structures. These make vanadium oxides attracting materials due to their rich electronic and magnetic structures as well as phase transitions. V_2O_3 is one of many transition metal oxides that present a distinct metal–insulator transition (MIT) [7]. In particular, the MIT of V_2O_3 is triggered by changes in temperature, doping components and concentration, and applied external pressure. Pure V_2O_3 goes from an antiferromagnetic insulator phase below 150–170 K to a paramagnetic metal phase at higher temperature [8–10]. This is usually considered the paradigm of the Mott-Hubbard transition, where the Coulomb interaction between conduction electrons leads to a breakdown of conventional one-electron band theory [11,12].

The binary V_2O_3–Fe_2O_3 solid solution system exhibits corundum structure, which shows interesting magnetic properties and gives further insight into the phenomenon of direct cation–cation interactions. It was also reported that when SnO_2 and Fe_2O_3 were added to V_2O_3-based PTC ceramic materials, they are reduced to corresponding metals under reductive atmosphere, which helps develop the sintering properties and reduce the room temperature properties. Therefore, it can be used in large electric power systems as current limiter materials [13]. The V_2O_3-α-Fe_2O_3 solid solution was normally synthesized through high temperature solid state reaction for a certain

*Corresponding author. Tel.: +1 412 396 4166; fax: +1 412 396 4829.
E-mail address: sorescu@duq.edu (M. Sorescu).

0272-8842/$ - see front matter © 2013 Elsevier Ltd and Techna Group S.r.l. All rights reserved.
http://dx.doi.org/10.1016/j.ceramint.2013.04.026

amount of time under vacuum, followed by quenching the obtained ingots in air [14]. So far, most of research interests in this system are focused on the metal–insulator transition behavior at low temperature. To the best of our knowledge, no detailed thermal, magnetic, or crystalline structure studies on $xV_2O_3 \cdot (1-x)Fe_2O_3$ solid solutions at room temperature with different molar ratios x are reported, especially for mechanochemical ball milling synthesized solid solutions.

In this work, we report the successful synthesis of $xV_2O_3 \cdot (1-x)Fe_2O_3$ solid solution by mechanochemical activation method through ball-milling of V_2O_3 and α-Fe_2O_3 mixtures with V_2O_3 molar concentration $x=0.1$, 0.3, 0.5, and 0.7 at room temperature. X-ray powder diffraction, simultaneous DSC–TGA, Mössbauer spectroscopy, scanning electron microscopy, and UV–vis spectroscopy have been employed to investigate the phase evolutions, thermal behaviors, magnetic properties and morphologies of ball-milled oxides at different ball-milling duration. The assisting role of mechanochemical activation in the synthesis of the V_2O_3-α-Fe_2O_3 solid solution is discussed.

2. Experimental

Vanadium (III) and iron (III) oxides were purchased from Alfa Aesar: Vanadium (III) oxide (95% metals basis, average particle size about 67.8 nm), and hematite (α-Fe_2O_3, 99% metal basis, average particle size about 49.2 nm). Powders of hematite and vanadium (III) oxides were milled in a hardened steel vial with 12 stainless-steel balls (type 440; eight of 0.25 in diameter and four of 0.5 in diameter) in the SPEX 8000 mixer mill for time periods ranging from 2 to 12 h. The ball/powder mass ratio was 5:1. Prior to their introduction in the ball milling device, the powders were manually ground in air to obtain a homogeneous mixture.

The X-ray powder diffraction patterns of samples were obtained using a PANalytic X′Pert Pro MPO powder diffractometer with CuKα radiation (45 kV/40 mA, $\lambda=1.54187$ Å) with a nickel filter on the diffracted side. A silicon-strip detector called X′cellerator was used. The scanning range was 10–80° (2θ) with a step size of 0.02°. The average particle size was determined by the Scherrer method. The lattice parameters were extracted from Rietveld structural refinement of the XRD patterns.

Simultaneous DSC–TGA experiments were performed using a Netzsch Model STA 449 F3 Jupiter instrument with a Silicon Carbide (SiC) furnace. Samples were contained in an alumina crucible with an alumina lid. Series of experiments were performed using 20 ± 2 mg sample size. The atmosphere consisted of flowing protective argon gas at a rate of 50 ml/min. DSC and TGA curves were obtained by heating samples from room temperature to 800 °C with a ramp rate of 10 °C/min. Both DSC and TGA curves were corrected by subtraction of a baseline which was run under identical conditions as DSC–TGA measurement with residue of samples in the crucible. The Netzsch Proteus Thermal Analysis software was used for DSC and TGA data analysis.

Room temperature transmission Mössbauer spectra were recorded using an MS-1200 constant acceleration spectrometer with a 10 mCi ^{57}Co source diffused in Rh matrix. Least-squares fittings of the Mössbauer spectra were performed with the NORMOS program.

Scanning electron microscopy was performed using a Hitachi S-3400N scanning electron microscope. The powders of both 12 h ball-milled sample were adhered on top of double side carbon tape which was attached onto a standard aluminum stub and examined under high vacuum conditions, respectively. Different accelerating voltages for different magnifications and a 5.0 mm working distance were employed.

An optical diffuse reflectance spectrum was obtained using a Varian Cary 5000 UV/vis/NIR spectrophotometer. The sample was loaded into a Harrick Praying Mantis diffuse reflectance accessory that uses elliptical mirrors. $BaSO_4$ was used as a 100% reflectance standard. Scans were performed from 2500 to 200 nm at a rate of 600 nm/min. The wavelength data were converted to electron volts, and the percent reflectance data were converted to absorbance units using the Kubelka–Munk equation [15].

3. Results and discussion

3.1. XRD

Fig. 1 represents the XRD patterns of V_2O_3-doped hematite, $xV_2O_3 \cdot (1-x)$α-Fe_2O_3 for $x=0.5$, corresponding to milling times between 2 and 12 h. The starting materials were pure α-Fe_2O_3 and V_2O_3 phases, and no diffraction peak from other phases was detected after the physically mixing process (Fig. 1a). For the ball-milled composites (Fig. 1b–e), the XRD patterns show progressive peak broadening with milling time. This peak broadening is associated with the decrease in grain sizes for both α-Fe_2O_3 and V_2O_3 samples. It can also be seen that the diffraction peak intensities of α-Fe_2O_3 and V_2O_3 decrease with the increase in ball-milling time, indicating the possible ion substitutions between V^{3+} and Fe^{3+} in the corresponding hematite and V_2O_3 lattices. However, both α-Fe_2O_3 and V_2O_3 phases are still present in the composites when the ball milling time is≤8 h, which can be identified from the splitting of the diffraction peaks. Both α-Fe_2O_3 and V_2O_3 phases are absent in the XRD patterns up to 12 h of milling time, and the split diffraction peaks merge together, indicating the formation of a solid solution of α-Fe_2O_3–V_2O_3 under mechanochemical activation up to 12 h. It has to be noted that the formation of solid solution cannot be excluded when the ball milling time is less than 8 h, however, these formed solid solutions can be fitted with either α-Fe_2O_3 or V_2O_3 phases. Table 1 presents the lattice parameters of the Rietveld structural refinement. It can be seen that the average grain size of α-Fe_2O_3 and V_2O_3 decreases with the ball-milling time. The original α-Fe_2O_3 has an average grain size of 49.2 nm and decreases to 31.6 nm after 2 h of ball milling. It decreases continuously at long ball milling times, from 24.2 nm for 4 h milling down to 18.5 nm for 8 h milling. The original V_2O_3 has an average grain size of 67.8 nm, and it

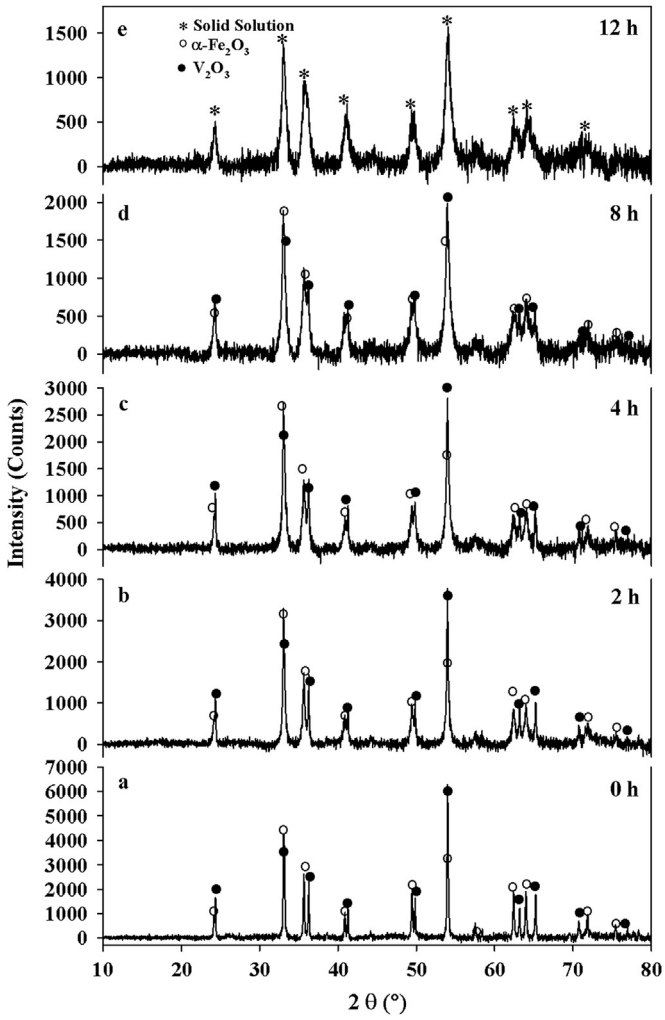

Fig. 1. XRD patterns of mechanochemically activated $xV_2O_3 \cdot (1-x)\alpha\text{-}Fe_2O_3$ ($x=0.5$) composites at ball milling time of: (a) 0 h; (b) 2 h; (c) 4 h; (d) 8 h; (e) 12 h, respectively.

drops to 45.9 nm after first 2 h of ball-milling time. It also decreases with the increase in ball milling times, from 27.2 nm for 4 h milling down to 16.5 nm for 8 h milling. The difference in the decrease in the average grain sizes of α-Fe_2O_3 and V_2O_3 may arise from the different micro-strains which were applied in the two different materials during the ball-milling process. After 12 h of ball milling, the average grain size of the formed solid solution is about 11.5 nm.

The variations in lattice parameters of hematite (*a* and *c*) and V_2O_3 (*a* and *c*) of $xV_2O_3 \cdot (1-x)\alpha\text{-}Fe_2O_3$ ($x=0.5$) composites are due to the high energy ball milling which causes the decrease in grain size, the gradual V^{3+} substitution of Fe^{3+} in hematite lattice, and Fe^{3+} substitution of V^{3+} in V_2O_3 lattice. For V_2O_3 phase, lattice parameter *a* increase from 4.9543 Å in 0 h ball-milled sample to 4.9881 Å in 8 h ball-milled sample, while lattice parameter *c* decreases from 14.0000 Å, to 13.9335 Å. The increase in the lattice parameter *a*, and the decrease in *c* of the V_2O_3 with the increase in ball-milling time is consistent with the radius difference between Fe^{3+} and V^{3+}, with Fe^{3+} (~ 0.63 Å) bigger than V^{3+} (~0.54 Å). Interestingly,

Table 1
Rietveld refinement parameters from XRD patterns of $xV_2O_3 \cdot (1-x)\alpha\text{-}Fe_2O_3$ ($x=0.5$) composites at different ball-milling times and the as-synthesized solid solution sample.

BMT (h)	Phase H = α-Fe_2O_3 V = V_2O_3	Lattice parameters			Grain size (nm)
		a (Å)	*c* (Å)	*V* (Å^3)	
0	H	5.0373	13.739	301.92	49.2
	V	4.9543	14	297.24	67.8
2	H	5.0346	13.7436	301.68	31.6
	V	4.9549	14	297.65	45.9
4	H	5.0316	13.7164	300.72	24.2
	V	4.9609	13.9998	298.37	27.2
8	H	5.0266	13.7339	300.51	18.5
	V	4.9881	13.9335	300.22	16.5
12	Solid solution	5.0073	13.8321	300.34	11.5
Error		± 0.0002	± 0.0002	± 0.01	± 0.1

lattice parameter *a* of α-Fe_2O_3 phase decreases with the increase of the ball-milling time, from 5.0373 Å for 0 h ball-milled sample to 5.0266 Å for 8 h milled sample. Parameter *c* does not change much during the milling process due to the similar *c* values in hematite and the formed solid solution. The change in the lattice parameters of α-Fe_2O_3 is due to the high energy ball-milling effects, which decrease the grain size during the ball-milling process, as well as the V^{3+} substitution of Fe^{3+} in α-Fe_2O_3 lattice. During the ball-milling process, a microstrain concentrates in the lattice and increases the lattice distortion and strain energy. The increase in the lattice distortion, decrease in grain size and ion substitutions result in the variation of lattice parameters of both α-Fe_2O_3 and V_2O_3. In fact, it is well documented in the literature that lattice parameter changes under ball-milling process, either contraction or expansion, are expected when the grain sizes decrease as compared to the values of bulk materials [16,17].

From the variations in lattice parameters and average grain sizes of α-Fe_2O_3 and V_2O_3, it can be inferred that the mechanochemical activation of the α-Fe_2O_3–V_2O_3 mixtures reduces the average grain sizes and introduces the ion substitutions between V^{3+} and Fe^{3+} in α-Fe_2O_3/V_2O_3 lattices and the continuous formation of α-Fe_2O_3–V_2O_3 solid solution. When the ball milling time is up to 12 h, a complete solid solution forms under mechanochemical activations. After continuous ball-milling up to 14 h, no further phase change was observed, indicating that 12 h ball milling time is enough to produce complete solid solution of $xV_2O_3 \cdot (1-x)Fe_2O_3$ (x=0.5).

Fig. 2 shows the X-ray powder diffraction patterns of the formed xV_2O_3–$(1-x)Fe_2O_3$ solid solutions with different V_2O_3 molar fractions *x* in the range of $0 \le x \le 1$ after 12 h ball milling time. Fig. 2a is a typical powder diffraction pattern of single-phase α-Fe_2O_3. The XRD pattern of the original V_2O_3 material is shown in Fig. 2f, and it is verified to be single phase. All of the formed solid solutions have the average grain size of ~12 nm, as evidenced from the similar intensities and widths in corresponding diffraction peaks. Compared to the XRD

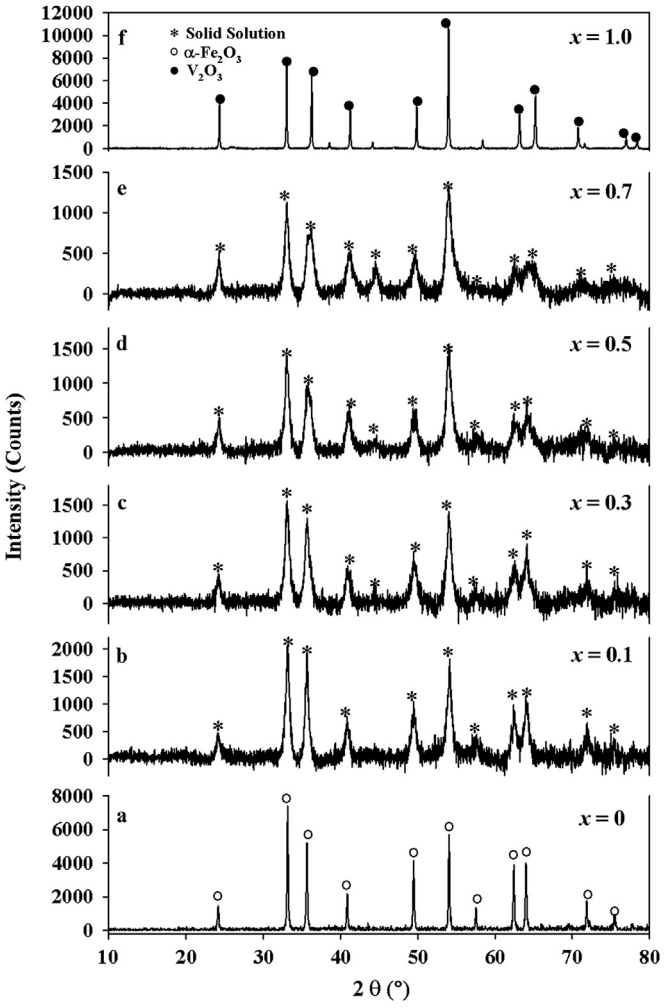

Fig. 2. XRD patterns of the synthesized $xV_2O_3 \cdot (1-x)\alpha\text{-}Fe_2O_3$ solid solution materials with different V_2O_3 molar fraction x of: (a) 0, (b) 0.1, (c) 0.3, (d) 0.5, (e) 0.7, and (f) 1, after 12 h of ball milling.

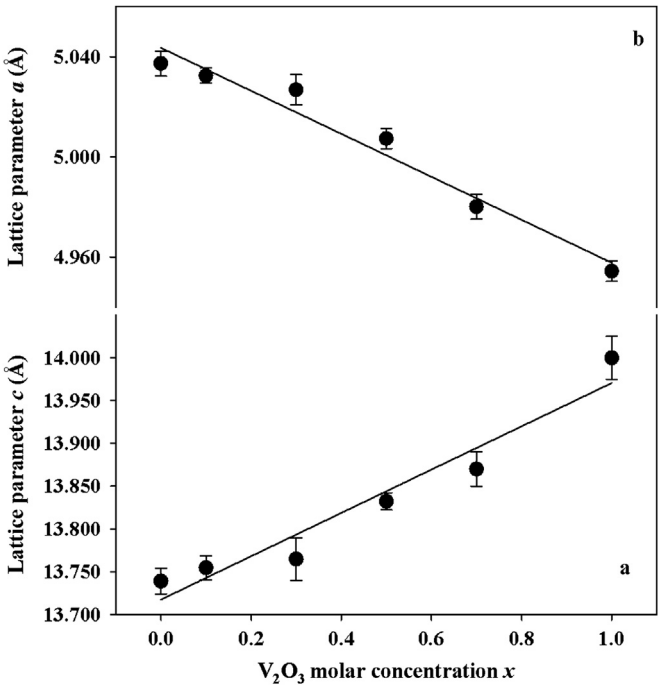

Fig. 3. Lattice parameters a and c of the formed $xV_2O_3 \cdot (1-x)\alpha\text{-}Fe_2O_3$ solid solutions as a function of V_2O_3 molar fraction x (a) lattice parameter a, and (b) lattice parameter c.

patterns of the original Fe_2O_3 corundum material (Fig. 2a), it was found that the diffraction peaks of the formed solid solutions shift to higher 2θ angles systematically with the increase in the molar fraction x of V_2O_3, owing to the difference in radius between $Fe^{3+}$and V^{3+}. The decrease in the unit cell volume V of the as-obtained solid solution with the increase in the V^{3+} content is also suggested, V drops from 302.11 Å^3 for $x=0.1$ to 297.91 Å^3 for $x=0.7$. Fig. 3 shows the variation of the lattice parameters a and c of the formed solid solutions, which were extracted from the Rietveld structural refinement of the XRD patterns, as a function of the V_2O_3 molar fraction x. It was found that there is a linear relationship between a, c and x, respectively. Lattice parameter a decreases from 5.0373 Å to 4.9801 Å, while c increases from 13.7390 Å to 13.8699 Å for $x=0$ and $x=0.7$, respectively. The linear relationship follows the Végard's rule [18,19], such that the lattice parameters a and c of the formed solid solution have weighted averages of those of the two end members [20]. The decrease in the relative amount of $\alpha\text{-}Fe_2O_3$ and the increase in V_2O_3 content result in smaller lattice parameter a and larger lattice parameter c of the solid solution xV_2O_3–$(1-x)Fe_2O_3$.

The linear changes in lattice parameters a and c are induced by the V^{3+}–Fe^{3+} ionic substitution, which in turn causes the formation of solid solutions. The different variation trends in lattice parameters a and c of the solid solutions can also be identified from the relative intensity changes of the diffraction peaks of ~33.1° and 54.0° with plane index as (114) and (116), respectively.

3.2. Mössbauer spectroscopy

Fig. 4(a)–(e) shows the room temperature transmission Mössbauer spectra of the $xV_2O_3(1-x)\alpha\text{-}Fe_2O_3$ ($x=0.5$) composites after ball milling for 0, 2, 4, 8 and 12 h, respectively. The hyperfine parameters corresponding to these spectra are given in Table 2. At 0 h of milling time, the spectrum was fitted with 1 sextet (Fig. 4a), corresponding to $\alpha\text{-}Fe_2O_3$. After 2 h of milling time, the Mössbauer spectrum was fitted with 3 sextets and 1 doublet. The three sextets can be attributed to the $\alpha\text{-}Fe_2O_3$ phase and the vanadium-substituted $\alpha\text{-}Fe_2O_3$ phase with V^{3+} substitution of Fe^{3+} in the $\alpha\text{-}Fe_2O_3$ lattice, respectively, and the doublet can be assigned to Fe^{3+} ions which substitute V^{3+} in the V_2O_3 lattice. When part of V^{3+} substitutes Fe^{3+} in $\alpha\text{-}Fe_2O_3$ lattice, antiferromagnetic ordering among Fe^{3+} can still be induced by exchange interaction, which gives sextets in the Mössbauer spectrum, with different strengths in hyperfine magnetic fields. However, when a small amount of Fe^{3+} substitution of V^{3+} in V_2O_3 lattice occurs, no antiferromagnetic ordering among Fe^{3+} in V_2O_3 lattice can be induced by the exchange interaction, therefore, only a quadrupole doublet appears. The isomer shift of Fe^{3+} extracted from the doublet is higher compared to that of Fe^{3+} extracted from

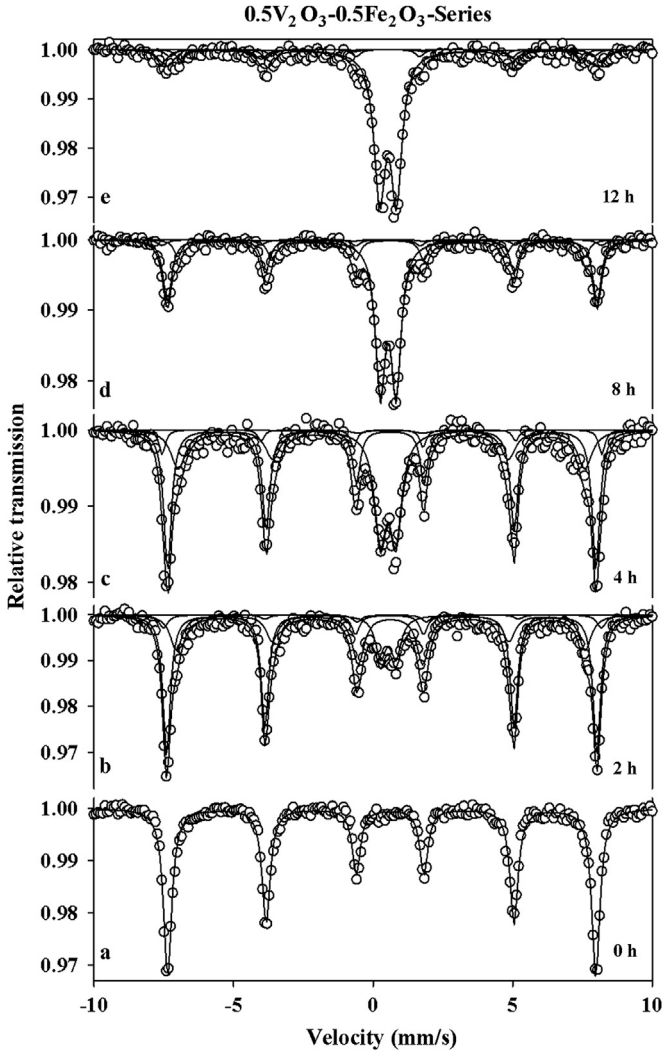

Fig. 4. Mössbauer spectra of mechanochemically activated $xV_2O_3 \cdot (1-x)\alpha$-$Fe_2O_3$ ($x=0.5$) composites at ball milling time of: (a) 0 h; (b) 2 h; (c) 4 h; (d) 8 h; (e) 12 h.

the sextet pattern of α-Fe_2O_3 phase, and this may be attributed to the change of neighbors in these two different cases. The relative abundance of a magnetic phase with highest hyperfine field (48.6 T) is 5.3%, and the relative population of a magnetic phase with lower hyperfine fields of 47.7 and 45.4 T is 50.8% and 33.2%, spectively.

After 12 h of milling time, the spectrum can still be fitted with 3 sextets and 1 doublet (Fig. 4e). Similar to the 2 h ball-milled sample, the three sextets can be attributed to the α-Fe_2O_3 phase and the vanadium-substituted α-Fe_2O_3 phase with V^{3+} substitution of Fe^{3+} in the α-Fe_2O_3 lattice, respectively, and the doublet can be assigned to Fe^{3+} ions which substitute V^{3+} in the V_2O_3 lattice. In addition, the population of this quadrupole splitting doublet component increases dramatically from 10.7% for 2 h ball-milled sample to 70.7% for 12 h ball-milled sample, indicating that longer ball-milling time introduces not only smaller grain sizes, but also more ion substitutions between Fe^{3+} and V^{3+}. It has to be noted that the population of the quadrupole split doublet increases with the increase of ball milling time, indicating the continuous

Table 2
Mössbauer parameters for $xV_2O_3 \cdot (1-x)\alpha$-$Fe_2O_3$ ($x=0.5$) composites at different ball-milling times.

Sample (x)	BMT (h)	I.S. (mm/s)	Q.S. (mm/s)	B (Tesla)	Abundance (%)
$x=0.5$	0	0.46	−0.30	47.5	100
	2	0.50	−0.32	48.6	5.3
		0.45	−0.27	47.7	50.8
		0.45	−0.35	45.4	33.2
		0.54	0.55	/	10.7
	4	0.43	−0.22	48.8	6.8
		0.46	−0.29	47.5	46.6
		0.46	−0.32	45.1	21.8
		0.53	0.55	/	24.8
	8	0.42	−0.23	48.7	3.9
		0.46	−0.27	47.7	35.1
		0.41	−0.22	45.2	11.1
		0.54	0.56	/	49.9
	12	0.41	−0.23	48.6	12.1
		0.43	−0.26	47.0	7.9
		0.39	−0.25	44.5	9.3
		0.53	0.60	/	70.7
Errors		**±0.01**	**±0.02**	**±0.5**	**±0.5**

Notes: BMT - Ball milling time; I.S. - Isomer shift (relative to the source); Q.S. - Quadrupole splitting/shift; B - Hyperfine magnetic field.

formation of solid solution. From the XRD pattern of this 12 h ball-milled sample, no hematite or V_2O_3 phases were detected, and the solid solution of Fe_2O_3–V_2O_3 was the only phase within the detection limits of XRD. The Mössbauer spectrum of the synthesized $xV_2O_3 \cdot (1-x)\alpha$-$Fe_2O_3$ ($x=0.5$) solid solution consists of three sextets and one doublet, indicating the co-existence of ferromagnetic and paramagnetic behavior. The ferromagnetic components may arise from the defects of the synthesized solid solution or the non-uniformly distributed Fe_2O_3 and V_2O_3 phases. The ferromagnetic behavior was also observed for $xV_2O_3 \cdot (1-x)\alpha$-$Fe_2O_3$ ($x=0.5$) solid solution synthesized through high temperature (~1400 °C) solid state reaction [21].

In order to investigate the magnetic properties of the $xV_2O_3 \cdot (1-x)\alpha$-$Fe_2O_3$ solid solutions with different V_2O_3 molar fractions x (0.1, 0.3, 0.5 and 0.7), Mössbauer measurements were performed, the spectra are shown in Fig. 5 and the fitting parameters are summarized in Table 3. All Mössbauer spectra of the formed solid solutions showed both sextets and doublet, indicating the co-existence of both ferromagnetic and paramagnetic properties. The percentage of paramagnetic components increases with the increase in V_2O_3 molar fraction x, owing to the decrease in exchange coupling between Fe^{3+} ions with the increase in V^{3+} concentration. However, the small amount of ferromagnetic components indicates that the solid solutions prepared through ball-milling possess defects, such that part of Fe^{3+} ions are still strongly coupled. The magnetic behavior of the ball-milled synthesized solid solution $xV_2O_3 \cdot (1-x)\alpha$-$Fe_2O_3$ is similar to that of solid-state-reaction synthesized V_2O_3–Fe_2O_3 solid solution with different V_2O_3

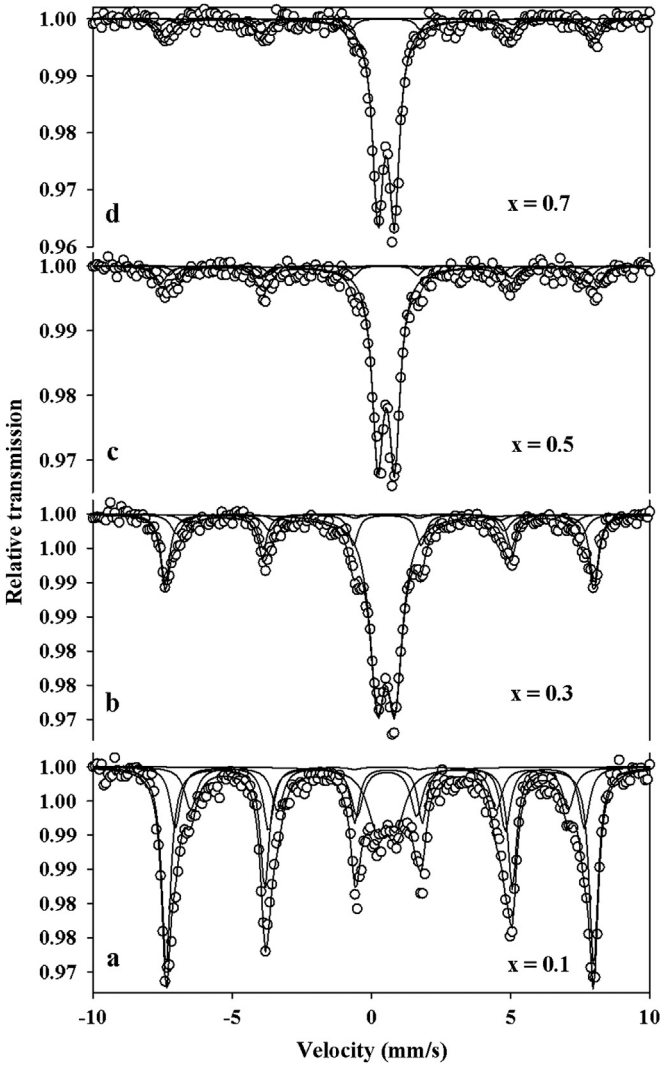

Fig. 5. Mössbauer spectra of the synthesized $xV_2O_3 \cdot (1-x)\alpha\text{-}Fe_2O_3$ solid solution materials with different V_2O_3 molar fraction x of: (a) 0.1, (b) 0.3, (c) 0.5, and (d) 0.7 after 12 h of milling, respectively.

Table 3
Mössbauer parameters for solid solution $xV_2O_3 \cdot (1-x)\alpha\text{-}Fe_2O_3$ with different V_2O_3 molar concentration x.

Sample (x)	BMT (h)	I.S. (mm/s)	Q.S. (mm/s)	B (Tesla)	Abundance (%)
$x=0.1$	12	0.46	−0.3	47.6	46.2
		0.43	−0.2	45.5	18.1
		0.42	−0.26	42	22.1
		0.53	0.71	–	13.6
$x=0.3$	12	0.43	−0.27	47.7	27.4
		0.43	−0.26	45.1	10.8
		0.45	−0.29	43.2	4.4
		0.53	0.63	–	57.4
$x=0.5$	12	0.41	−0.23	48.6	12.1
		0.43	−0.26	47	7.9
		0.39	−0.25	44.5	9.3
		0.53	0.6	–	70.7
$x=0.7$	12	0.4	−0.23	48.9	8.2
		0.4	−0.2	47.6	16.5
		0.39	−0.19	45.4	2.4
		0.53	0.59	–	72.9
Errors		**±0.01**	**±0.02**	**±0.5**	**±0.5**

Notes: BMT - Ball milling time; I.S.—Isomer shift (relative to the source); Q.S.—Quadrupole splitting/shift; B—Hyperfine magnetic field.

contents, such that the ferromagnetic, weak ferromagnetic properties and Curie temperature are heavily dependent on the molar ratios of V_2O_3 [22]. The existence of ferromagnetic behavior of the formed solid solutions may also be explained by the fact that Fe^{3+} ions participate in the long range order through V^{3+}–Fe^{3+} interaction [23].

3.3. Scanning electron microscopy

SEM was employed to study the morphology and particle size of the as-obtained solid solution. Fig. 6 shows secondary electron SEM images of the $xV_2O_3 \cdot (1-x)\alpha\text{-}Fe_2O_3$ ($x=0.5$) composite after 12 h of ball-milling time. For the 12 h ball-milled composites, a mixture of large crystal agglomerates in the size range 1 μm to 30 μm coated with much finer grains with nanometer dimensions is observed (Fig. 6a). However, most particles are still less than 10 μm at this magnification scale. Fig. 6b shows more details of the as-obtained solid solution at a different magnification. It can be seen clearly that the large agglomerates consist of fine grains with redundant sizes in nanometer range. Grains in the nanometer size range are distributed randomly and form the big agglomerates, indicating ball milling is a useful method to prepare composites in nanometer scale. Agglomerates were also found in ball-milling prepared $LaFeO_3$ perovskite materials [24], indicating it is a general phenomenon to produce some agglomerates with micrometer size using the high energy ball milling method.

The mapping analysis showed that V^{3+} substitution of Fe^{3+} in Fe_2O_3 lattice and Fe^{3+} substitution of V^{3+} in V_2O_3 lattice occurs simultaneously after 12 h ball milling time, and the O^{2+}, V^{3+} and Fe^{3+} are relative uniformly distributed in the synthesized solid solution (Fig. 7a-e). However, some Fe^{3+} rich areas can be also observed form Fe^{3+} map with bright brown dots (Fig. 7e), which may account for the ferromagnetic behavior of the synthesized solid solution that has three sextets in the Mössbauer spectrum (Fig. 5c). All these SEM images and mapping analysis point to that a well-mixed dispersion of V_2O_3–Fe_2O_3 solid solution with fine-scale grains was achieved by mechanochemical ball milling, though some large agglomerates also formed during the process.

3.4. Simultaneous DSC–TGA

The DSC–TGA curves of the original $\alpha\text{-}Fe_2O_3$ and V_2O_3 samples are shown in Fig. 8. One endothermic peak at 103 °C can be been seen for the original V_2O_3 sample (Fig. 8b). The TGA curve of the V_2O_3 sample shows that there is a distinguished weight loss (∼−4.5%) corresponding to the

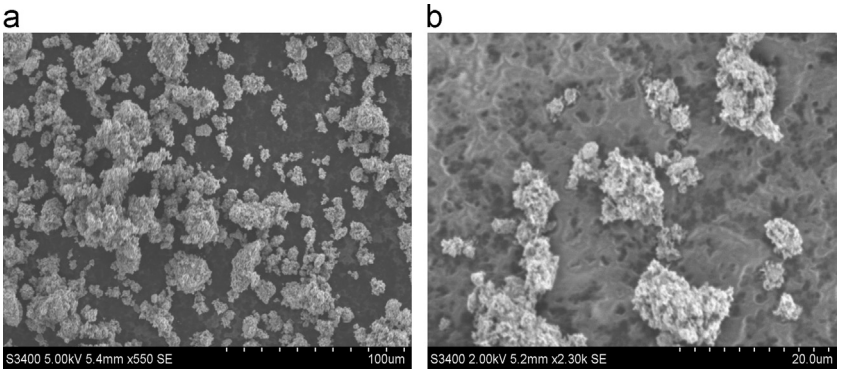

Fig. 6. SEM images of mechanochemically activated $xV_2O_3 \cdot (1-x)\alpha\text{-}Fe_2O_3$ ($x=0.5$) composites at ball-milling time of 12 h.

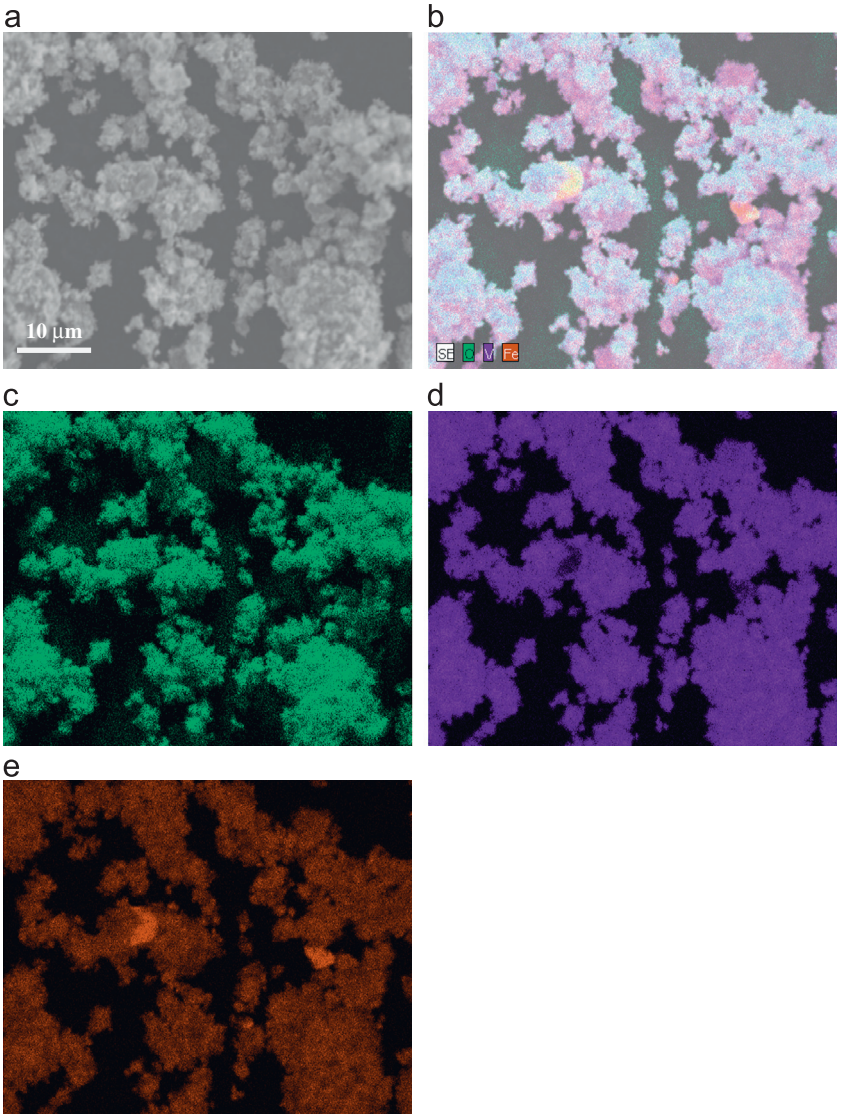

Fig. 7. Energy dispersive X-ray compositional images of the sample specimen area at the same magnification: (a) typical SEM image of agglomerate covered with fine particles; (b) Overall compositional image, (c) O K line image; (d) V L line image; and (e) Fe K line image.

endothermic peak at 103 °C, which can be assigned to the physically absorbed water content. No weight loss was observed for the V_2O_3 sample above 300 °C, indicating the thermal stability of this sample at high temperature. Several exothermic peaks from the DSC curve of V_2O_3 above 300 °C can be assigned to the crystallization of V_2O_3 fine particles.

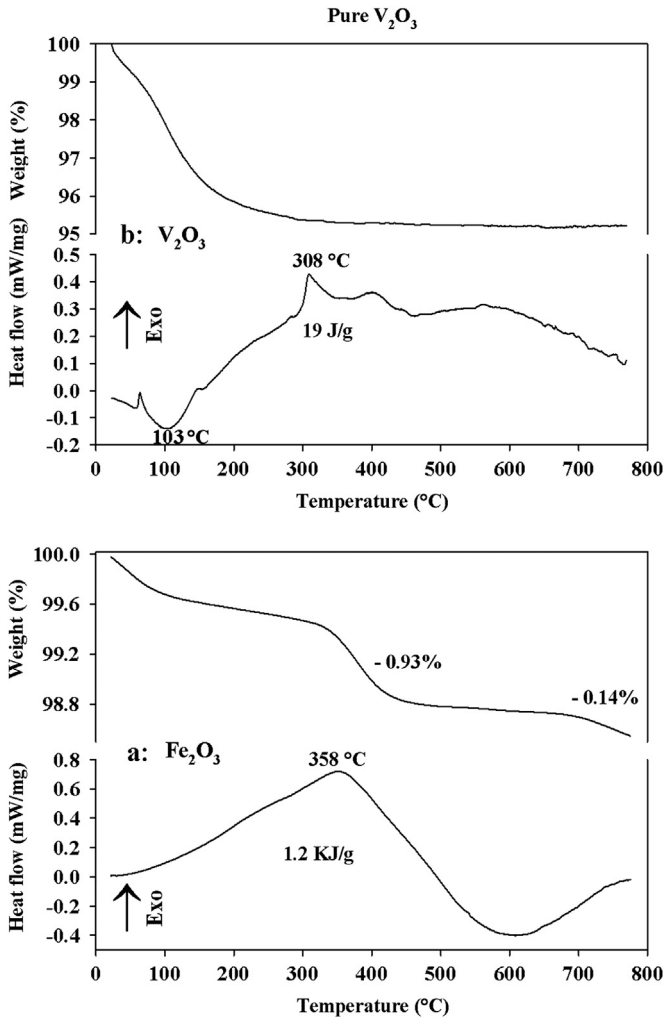

Fig. 8. DSC–TGA curves of the starting materials (a) α-Fe_2O_3, and (b) V_2O_3.

The detailed explanations of the DSC–TGA curves of the original α-Fe_2O_3 samples have been discussed in reference [25], with the first exothermic peak and weight loss corresponding to the decomposition of α-Fe_2O_3 under argon atmosphere.

Fig. 9 shows the DSC and TGA curves of $xV_2O_3 \cdot (1-x)$α-Fe_2O_3 ($x=0.5$) composites after ball milling for 0, 2, 4, 8 and 12 h, respectively. Similar to the weight loss of the original V_2O_3 sample, the weight loss up to temperatures of about 300 °C for all the ball-milled samples can be attributed to the surface physically adsorbed water.

At 0 h of milling time, the DSC curve showed one endothermic peak at 90 °C and one small exothermic peak (Fig. 9a) with the peak temperature at 311 °C. The endothermic peak can be assigned to desorption of water content. However, the characteristics of this DSC curve are not just the simple sum of the DSC curves of the original α-Fe_2O_3 and V_2O_3 samples. The integration of this exothermic peak gives an enthalpy value of 12 J/g, which is much smaller than that of the original α-Fe_2O_3 sample (~1.2 kJ/g) or V_2O_3 sample (19 J/g). This means that the manually ground mixture of $xV_2O_3 \cdot (1-x)$ α-Fe_2O_3 ($x=0.5$) shows a different thermal behavior compared to samples with α-Fe_2O_3 or V_2O_3 alone. The peak temperature of this exothermic peak (311 °C) shifted a little bit comparing with that of the original V_2O_3 sample (308 °C). The difference in DSC curves may characterize strong solid–solid interactions between α-Fe_2O_3 and V_2O_3, which affect the crystallization of α-Fe_2O_3 and V_2O_3 fine grains.

Fig. 9f shows the TGA curve of $xV_2O_3 \cdot (1-x)$α-Fe_2O_3 ($x=0.5$) composite for 0 h of ball milling. A weight loss value of 0.60% can be observed for temperatures from 330 to 400 °C, and this weight loss can be assigned to the thermal decomposition of α-Fe_2O_3 under Ar atmosphere. The value of this weight loss is smaller than that of the pure original α-Fe_2O_3 (0.93%) and is reasonable considering that there is 50% of V_2O_3 in molar fraction in the mixtures. This means that the manually grinding process does not dramatically change the phase transition of α-Fe_2O_3 decomposition. The decrease in the enthalpy for this sample must be due to the solid–solid interactions.

After ball milling for 2, 4, 8 and 12 h, the DSC curves of $xV_2O_3 \cdot (1-x)$α-Fe_2O_3 ($x=0.5$) nanostructure system (Fig. 9b–e) change dramatically compared to that of 0 h ball milled sample, indicating the strong effect of ball-milling on the thermal behavior of $xV_2O_3 \cdot (1-x)$α-Fe_2O_3 system. One broad endothermic peak with peak temperature around 100 °C can be observed for all of the ball-milled samples, which can be assigned to desorption of water contents. The small exothermic peak around 311 °C, which was observed for 2 h ball-milled sample, diminished for the ball-milled samples with longer ball milling time. Another exothermic peak (~500 °C) appears on the DSC curves of the ball-milled sample. The intensity of the exothermic peak on the DSC curves increases with the increase of the ball milling time. From the TGA curves of $xV_2O_3 \cdot (1-x)$α-Fe_2O_3 nanostructure system ($x=0.5$) after different ball-milling times (Fig. 9g–j), it was found that the amount of weight loss in the temperature range of 330 to 400 °C changes dramatically with the ball-milling time; no distinguished weight loss was observed for all of the ball-milled samples, indicating the stronger solid–solid interaction between α-Fe_2O_3 and V_2O_3 after ball-milling, compared to 0 h ball-milled sample. The difference in DSC and TGA curves is due to the continuous V^{3+}–Fe^{3+} substitution in the corresponding Fe_2O_3 and V_2O_3 lattices and it also reflects the continuous formation of solid solution between α-Fe_2O_3 and V_2O_3 phases, though the peak splitting is still present in the XRD patterns when the ball milling time is less than 8 h.

3.5. Optical diffuse reflectance spectroscopy

The optical diffuse reflectance spectrum for samples of Fe_2O_3, V_2O_3, and $xV_2O_3 \cdot (1-x)$α-Fe_2O_3 ($x=0.5$) with different ball milling times, are shown in Fig. 10.

For hematite, the valence and conduction bands arise from crystal field splitting of the Fe 3*d* levels due to the octahedral coordination of oxygen around Fe [26]. As shown in Fig. 10a, diffuse reflectance spectra of original hematite exhibit a band gap energy value of ~2.19 eV, which is consistent with reported value for bulk hematite [27,28]. V_2O_3 forms

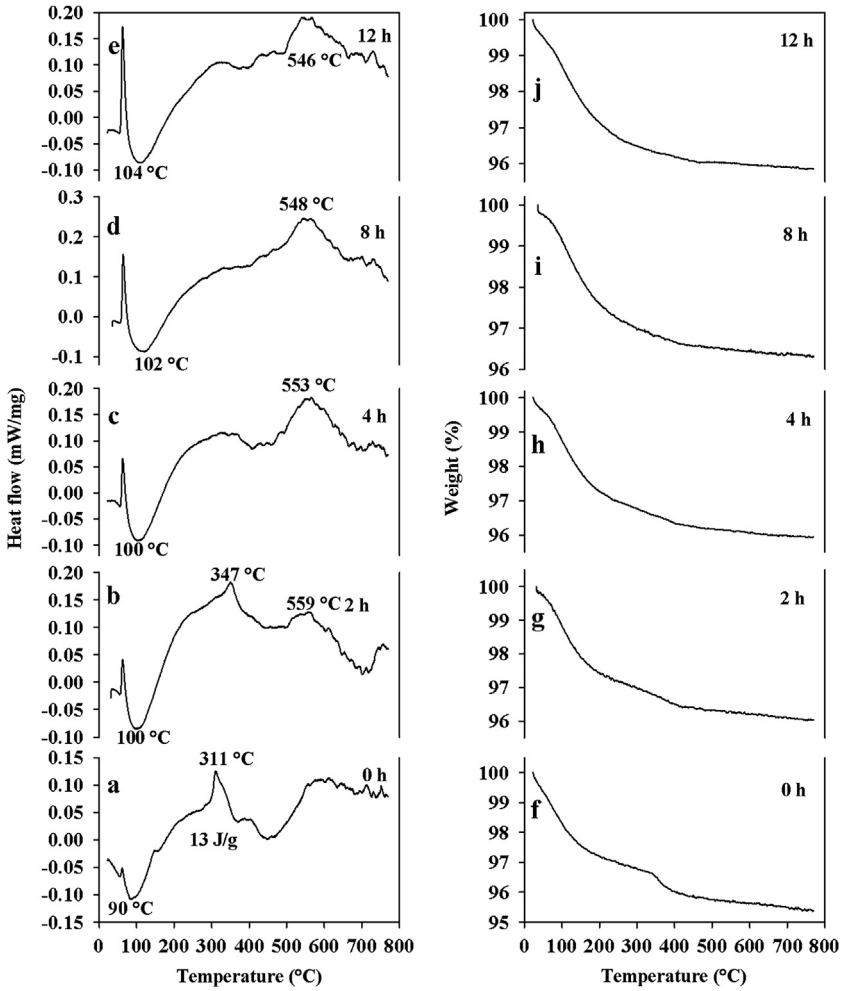

Fig. 9. DSC curves of mechanochemically activated $xV_2O_3 \cdot (1-x)\alpha\text{-}Fe_2O_3$ ($x=0.5$) composites at ball milling time of: (a) 0 h; (b) 2 h; (c) 4 h; (d) 8 h; (e) 12 h, and TGA curves of mechanochemically activated $xV_2O_3 \cdot (1-x)\alpha\text{-}Fe_2O_3$ composites ($x=0.5$) at ball milling time of: (f) 0 h; (g) 2 h; (h) 4 h; (i) 8 h; (j) 12 h.

corundum crystal with *cR3* space group, the band gap energy is rather complicated. V_2O_3 is metallic at room temperature, and no distinguished band gap can be observed in the range of 1.0 to 2.5 eV (Fig. 10b). However, there is a continuous increase in absorption of UV–vis light in the energy range of 2.5 to 3.26 eV, which reflects the complicated electron transition states in V_2O_3 material. For sample $xV_2O_3 \cdot (1-x)$ $\alpha\text{-}Fe_2O_3$ ($x=0.5$) with 0 h of milling time, in other words, just after physical mixing of V_2O_3 and $\alpha\text{-}Fe_2O_3$, the UV–vis spectrum changes slightly, with a relatively sharp increase in α/s at energy value of ~2.19 eV (Fig. 10c), which is similar to that of the original hematite. On the other hand, the continuous increase in the α/s value in the energy range of 2.28 to 4.85 eV comes from electron transitions of V_2O_3. The characteristics of UV–vis spectrum for this 0 h ball milled sample indicates that physical mixing doesnot dramatically change the band gap energies of Fe_2O_3 and V_2O_3, respectively.

After different hours of milling time, band gap energies of the ball-milled samples do change dramatically, especially for the 8 and 12 h ball milled samples (Fig. 10f and 10g). Similar to that of 0 h ball-milled samples, there is still relatively sharp increase in the α/s value at ~2.18 eV. However, the energy is continuously increasing as the α/s on the UV–vis spectra was narrowed to 3.34 eV, suggesting the strong solid–solid interaction between Fe_2O_3 and V_2O_3 phases as well as the formation of $xV_2O_3 \cdot (1-x)\alpha\text{–}Fe_2O_3$ ($x=0.5$) solid solution; this is in good agreement with the XRD results that diffraction peaks splitting diminished after 12 h of ball milling. The mechanochemical activation process does alter the band gap energies of the ball-milled oxide mixtures dramatically, which can also be reflected from the changes in its microstructures, average grain sizes, thermal stability, and magnetic properties. After 12 h ball milling, the formed $xV_2O_3 \cdot (1-x)\alpha\text{-}Fe_2O_3$ ($x=0.5$) solid solution has a semiconductor behavior, which is similar to hematite.

4. Conclusions

After mechanochemical activation of $\alpha\text{-}Fe_2O_3$ and V_2O_3 mixtures with 1:1 M ratio for 12 h, single phase solid solution was successfully synthesized by mechanochemically activated composite for 12 h. The mechanochemical activation process

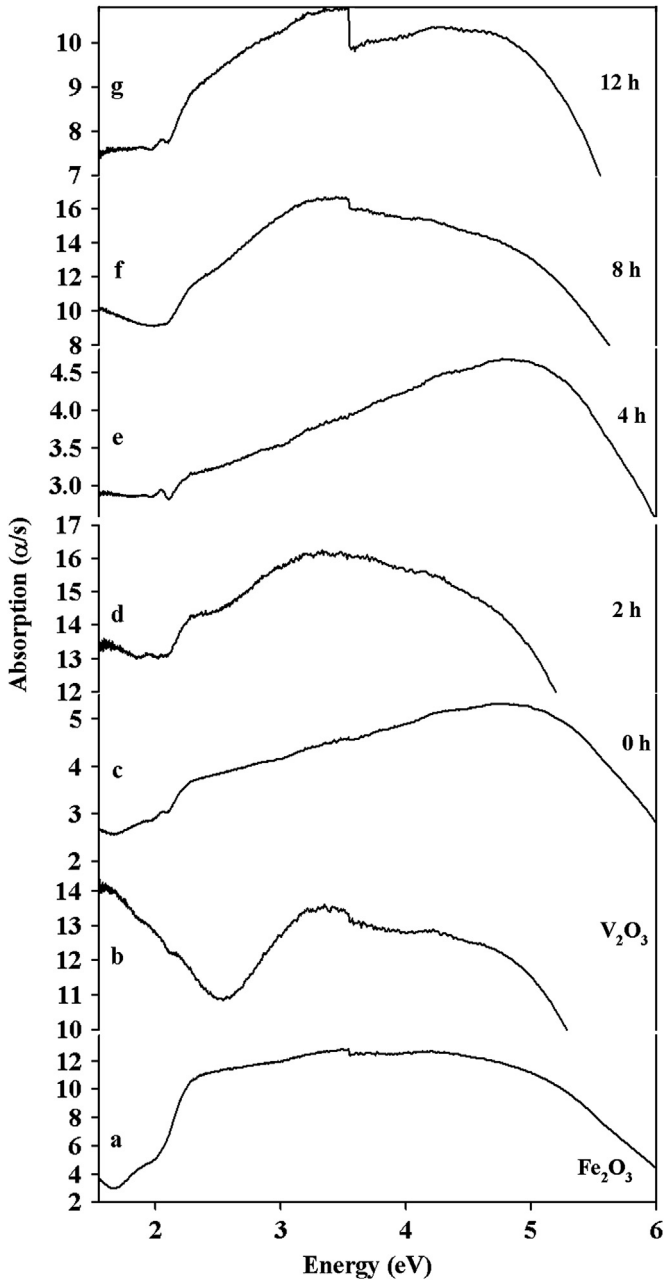

Fig. 10. The optical diffuse reflectance spectrum converted to absorption for samples: (a) original hematite, (b) original V_2O_3, and mechanochemically activated $xV_2O_3 \cdot (1-x)\alpha$-$Fe_2O_3$ ($x=0.5$) composites at ball milling time of: (c) 0 h; (d) 2 h; (e) 4 h; (f) 8 h; and (g) 12 h, respectively. On the y axis, α is the absorbance and s is the scattering coefficient constant.

played an important role for the synthesis of solid solution. It homogeneously mixed the starting materials of α-Fe_2O_3 and V_2O_3 and decreased their average grain sizes. The Mössbauer spectroscopy studies indicated that the spectrum of the mechanochemically activated composites consisted of three sextets and one doublet, indicating the occurrence of V^{3+}–Fe^{3+} ion substitutions in the corresponding α-Fe_2O_3 and V_2O_3 lattices, respectively. Simultaneous DSC–TGA studies indicated that the synthesized solid solution are thermally stable up to 800 °C. SEM images of the as-synthesized solid solutions confirmed the wide range distribution of particles sizes, from nanometer-sized particles to micrometer-sized agglomerates, but the grains maintain sizes at the nanometer scale. Optical diffuse reflectance spectroscopy studies showed that the synthesized solid solution phase had semiconductor properties.

Acknowledgments

This work was supported by the National Science Foundation under grant number DMR-0854794 and the National Science Foundation (NSF) Major Research Instrumentation (MRI) program under grant number CHE-0923183.

References

[1] G.X. Wang, X.L. Gou, J. Horvat, J. Park, Facile synthesis and characterization of iron oxide semiconductor nanowires for gas sensing application, Journal of Physical Chemistry C 112 (2008) 15220–15225.
[2] B. Raffaella, S. Etienne, G. Cinzia, G. Fabia, G.H. Mar, A.G. Miguel, C. Roberto, D.C. Pantaleo, Colloidal semiconductor/magnetic heterostructures based on iron-oxide-functionalized brookite TiO_2 nanorods, Physical Chemistry Chemical Physics 11 (2009) 3680–3691.
[3] S. Krishnamoorthy, J.A. Rivas, M.D. Amiridis, Catalytic oxidation of 1,2-dichlorobenzene over supported transition metal oxides, Journal of Catalysis 193 (2000) 264–272.
[4] M. Sorescu, L. Diamandescu, A. Tomescu, D. Tarabasanu-Mihaila, V. Teodorescu, Structure and sensing properties of $0.1SnO_2$–0.9-Fe_2O_3 system, Materials Chemistry and Physics 107 (2008) 127–131.
[5] B. Grzybowska-Swierkosz, Vanadia-Titania catalysts for oxidation of *o*-xylene and other hydrocarbons, Applied Catalysis A 157 (1997) 263–310.
[6] S. Suenev, M.G. Ramsey, F.P. Netzer, Vanadium oxide surface studies, Progress in Surface Science 73 (2003) 117–165.
[7] M. Imada, A. Fujimori, Y. Tokura, Metal–insulator transitions, Reviews of Modern Physics 70 (1998) 1039–1263.
[8] R.M. Moon, Antiferromagnetism in V_2O_3, Physical Review Letters 25 (1970) 527–529.
[9] J.B. Goodenough, Metallic oxides, Progress in Solid State Chemistry 5 (1971) 145–399.
[10] D. Weber, A. Stork, S. Nakhal, C. Wessel, C. Reimann, W. Hermes, A. Müller, T. Ressler, R. Pöttgen, T. Bredow, R. Dronskowski, M. Lerch, Bixbyite-type V_2O_3—a metastable polymorph of vanadium sesquioxide, Inorganic Chemistry 50 (2011) 6762–6766.
[11] F.J. Morin, Oxides which show a metal-to-insulator transition at the Néel temperature, Physical Review Letters 3 (1959) 34–36.
[12] R.J.O. Mossanek, M. Abbate, Importance of the V 3d–O 2p hybridization in the Mott-Hubbard material V_2O_3, Physical Review B 75 (2007) 115110-1–115110-5.
[13] L.J. Ruan, W.Q. Cui, Mössbauer study of iron in V_2O_3-based PTC ceramics, Journal of Materials Science Letters 16 (1997) 1231–1232.
[14] A. Wold, D. Rogers, R.J. Arnott, N. Menyuk, Vanadium iron oxides, Journal of Applied Physics 33 (1962) 1208–1209.
[15] P. Kubelka, F. Munk, Ein Beitrag zur Optik der Farbanstriche, Zeitschrift für Technische Physik 12 (1931) 593–601 English translated by Westin S.
[16] M. Sorescu, L. Diamandescu, Mechanochemical and magnetomechanical synthesis of hematite nanoparticles, Hyperfine Interact 196 (2010) 349–358.
[17] H. Dutta, S.K. Pradhan, Microstructure characterization of high energy ball-milled nanocrystalline V_2O_3 by rietveld analysis, Materials Chemistry and Physics 77 (2002) 868–877.
[18] L. Végard, Die Konstitution der Mischkristalle und die Raumfüllung der Atome, Zeitschrift für Physik 5 (1921) 17–26.
[19] U. Bleil, An experimental study of the titanomagnetite solid solution series, Pageoph 114 (1976) 165–175.

[20] B.C. Melot, K. Page, R. Seshadri, E.M. Stoudenmire, L. Balents, D.L. Bergman, T. Proffen, Magnetic frustration on the diamond lattice of the *A*-site magnetic spinels $CoAl_2$–xGa_xO_4: The role of lattice expansion and site disorder, Physical Review B 80 (2009) 104420.

[21] G. Shirane, D.E. Cox, S.L. Ruby, Mössbauer study of isomer shift, quadrupole interaction, and hyperfine field in several oxides containing Fe^{57}, Physical Review 125 (1962) 1158–1165.

[22] D.E. Cox, W.J. Takei, R.C. Miller, G. Shirane, A magnetic and neutron diffraction study of the Fe_2O_3-V_2O_3 system, Journal of Physics and Chemistry of Solids 23 (1962) 863–874.

[23] T. Shinjo, K. Kosuge, Mössbauer effect study of V_2O_3, Journal of the Physical Society of Japan 21 (1966) 2622–2626.

[24] M. Sorescu, T.H. Xu, J.D. Burnett, J.A. Aitken, Investigation of $LaFeO_3$ perovskite growth mechanism through mechanical ball milling of lanthanum and iron oxides, Journal of Materials Science 46 (2011) 6709–6717.

[25] M. Sorescu, T.H. Xu, L. Diamandescu, Synthesis and characterization of $x TiO_2$•$(1–x)$α-Fe_2O_3 magnetic ceramic nanostructure system, Materials Characterization 61 (2010) 1103–1118.

[26] F.J. Morin, Electrical properties of α-Fe_2O_3, Physical Review 93 (1954) 1195–1199.

[27] L.A. Marusak, R. Messier, W.B. White, Optical absorption spectrum of hematite, α-Fe_2O_3 near IR to UV, Journal of Physics and Chemistry of Solids 41 (1980) 981–984.

[28] M.P. Dare-Edwards, J.B. Goodenough, A. Hamnett, P.R. Trevellick, Electrochemistry and photoelectrochemistry of iron (III) oxide, Journal of the Chemical Society, Faraday Transactions 79 (1983) 2027–2041.